

Open camera or QR reader and
scan code to access this article
and other resources online.



3D Printed Acoustically Programmable Soft Microactuators

Murat Kaynak,* Amit Dolev,* and Mahmut Selman Sakar

Abstract

The concept of creating all-mechanical soft microrobotic systems has great potential to address outstanding challenges in biomedical applications, and introduce more sustainable and multifunctional products. To this end, magnetic fields and light have been extensively studied as potential energy sources. On the other hand, coupling the response of materials to pressure waves has been overlooked despite the abundant use of acoustics in nature and engineering solutions. In this study, we show that programmed commands can be contained on 3D nanoprinted polymer systems with the introduction of selectively excited air bubbles and rationally designed compliant mechanisms. A repertoire of micromechanical systems is engineered using experimentally validated computational models that consider the effects of primary and secondary pressure fields on entrapped air bubbles and the surrounding fluid. Coupling the dynamics of bubble oscillators reveals rich acoustofluidic interactions that can be programmed in space and time. We prescribe kinematics by harnessing the forces generated through these interactions to deform structural elements, which can be remotely reconfigured on demand with the incorporation of mechanical switches. These basic actuation and analog control modules will serve as the building blocks for the development of a novel class of micromechanical systems powered and programmed by acoustic signals.

Keywords: microactuators, soft robotics, acoustics, bistable mechanisms, physical intelligence, 3D printing

Introduction

SOFT MATERIALS CAN be programmed to change their physical properties such as shape and stiffness on-the-fly by the externally applied light, heat, mechanical forces, or magnetic fields.^{1–5} Such material formulations have great potential, particularly at small scales, to achieve functionalities that are unattainable by conventional mechatronic systems.^{6–13} Notably, simple mechanical structures fabricated from magne-

torheological or liquid crystal elastomers displayed a virtually unlimited number of degrees of freedom (DOF), as a result of either the spatial complexity of the magnetization profile^{14–16} or the use of structured illumination.^{17,18} Moreover, rationally designed flexible structures, also known as mechanical metamaterials, can realize programmable digital logic.^{19–29} This route for physical intelligence has already been pursued by living organisms,^{30–32} and extensively studied for the development of autonomous soft robots.^{33–36}

Institute of Mechanical Engineering, Ecole Polytechnique Fédérale de Lausanne, Lausanne, Switzerland.

*These authors contributed equally to this work.

© Murat Kaynak *et al.* 2022; Published by Mary Ann Liebert, Inc. This Open Access article is distributed under the terms of the Creative Commons Attribution Noncommercial License [CC-BY-NC] (<http://creativecommons.org/licenses/by-nc/4.0/>) which permits any non-commercial use, distribution, and reproduction in any medium, provided the original author(s) and the source are cited.

Acoustofluidics has several unique properties that can reveal the full potential of programmable soft matter. Air bubbles are efficient transducers that generate forces through interactions with the external pressure waves, the surrounding fluid, and with each other.^{37–45} Therefore, these interactions can be programmed by modulating the acoustic wave as well as the geometry and the spatial distribution of bubbles. The generated forces are determined by primary and secondary acoustic effects that are highly nonlinear. Thus, a detailed understanding of the underlying physics is instrumental to using air bubbles for controlling deformable elements. To address this unmet challenge, we combined analytical modeling, finite element simulations, and experimental analysis that involved detailed characterization of acoustic pressure, bubble oscillations, and forces generated by bubbles with coupled dynamics.

In this study, we present an integrated design, fabrication, and control methodology that transforms monolithically printed flexible structures into programmable soft robotic systems. The key innovation is the spatial patterning of polymer capsules that stably contain individual air bubbles along ultraflexible beams using direct laser writing (Fig. 1a, Supplementary Fig. S1 and Supplementary Movie S1). By tuning the geometry of the capsules and the architecture of the material, we precisely controlled the acoustofluidic interactions (Fig. 1b, c). We demonstrate the compatibility of our acousto-active systems with mechanical logic by constructing actuated bistable mechanisms.

Results and Discussion

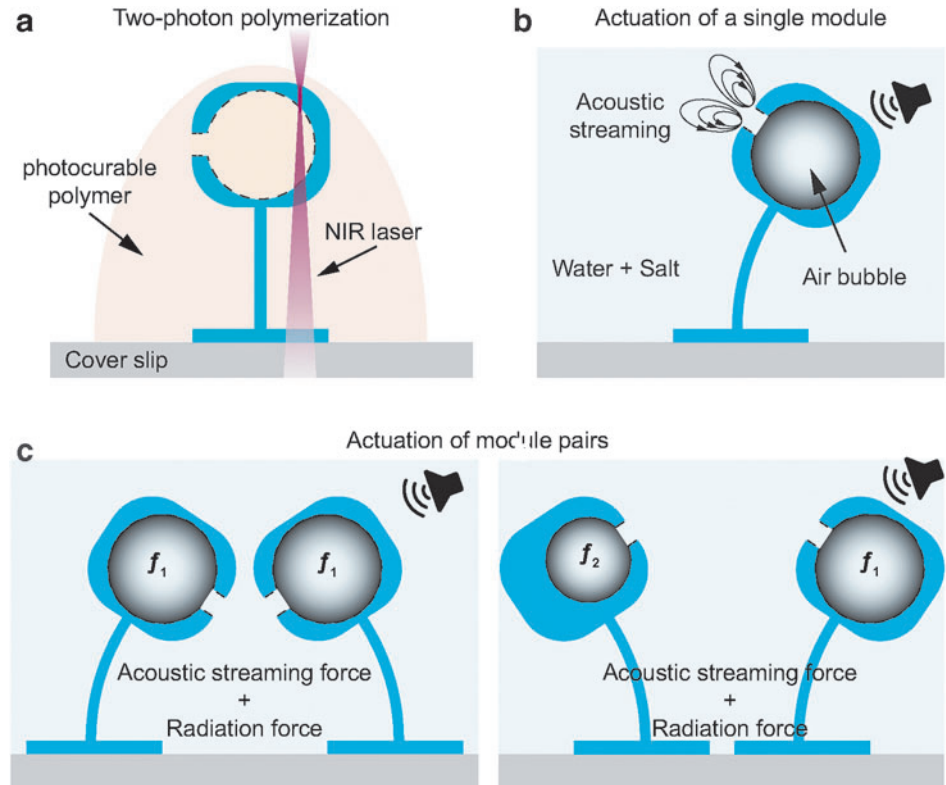
The basic actuator module consists of a 3D printed cylindrical capsule with a single circular orifice (Fig. 2a). A similar

manufacturing technique and geometry has been recently used to generate polymer microparticles with liquid-phase core.⁴⁶ We printed all the structures as a monolithic piece from a single biocompatible soft polymer, trimethylolpropane ethoxylate triacrylate (TPETA),⁴⁷ using two-photon polymerization (Fig. 2b). A detailed description of the experimental methods and control system, including the peripheral electronics is provided in Supplementary Note S1 and pictured in Supplementary Figure S9. Within this capsule, the bubble is physically isolated from the surrounding fluid except at the side of the opening (Fig. 2c). Acoustic excitation of a single bubble submerged in liquid generates microstreaming.⁴⁸ By entrapping bubbles inside cavities, their oscillations are constrained to regions defined by the orifices.

In this configuration, acoustic streaming generated counter-rotating vortices and a jet localized in the center, which was captured using high-speed recordings of tracer particles around the actuator module (Fig. 2d). Once an actuator is connected to a cantilever beam, it is expected to generate thrust normal to the orifice's plane, thereby deforming the beam. By carefully tuning the acoustic frequency, different vibration modes of the coupled fluid-structure system can be excited.⁴⁹ The vibration modes are manifested by the unique deformation patterns of the bubble at the interface. Nevertheless, we focused our attention on the first mode because, assuming a uniform distribution, the projection of the impinging pressure is maximal.

Large deformation and complex motion can be generated with slender structural elements, including beams, plates, and shells.^{50–52} We have recently developed an analytical model that calculates the natural frequencies and corresponding vibration modes of bubbles entrapped inside arbitrarily shaped cavities with multiple circular orifices.⁴⁹ In brief, we

FIG. 1. Conceptual illustration of the presented methodology. **(a)** Actuator modules (i.e., capsules with entrapped air bubbles) are nanoprinted using two-photon polymerization technique. Two different acoustic actuation scenarios are systematically studied. **(b)** A single actuator module is excited at the natural frequency to deform ultraflexible structures. **(c)** Pairs of identical or distinct actuator modules are excited at various frequencies to generate attractive and repulsive forces.



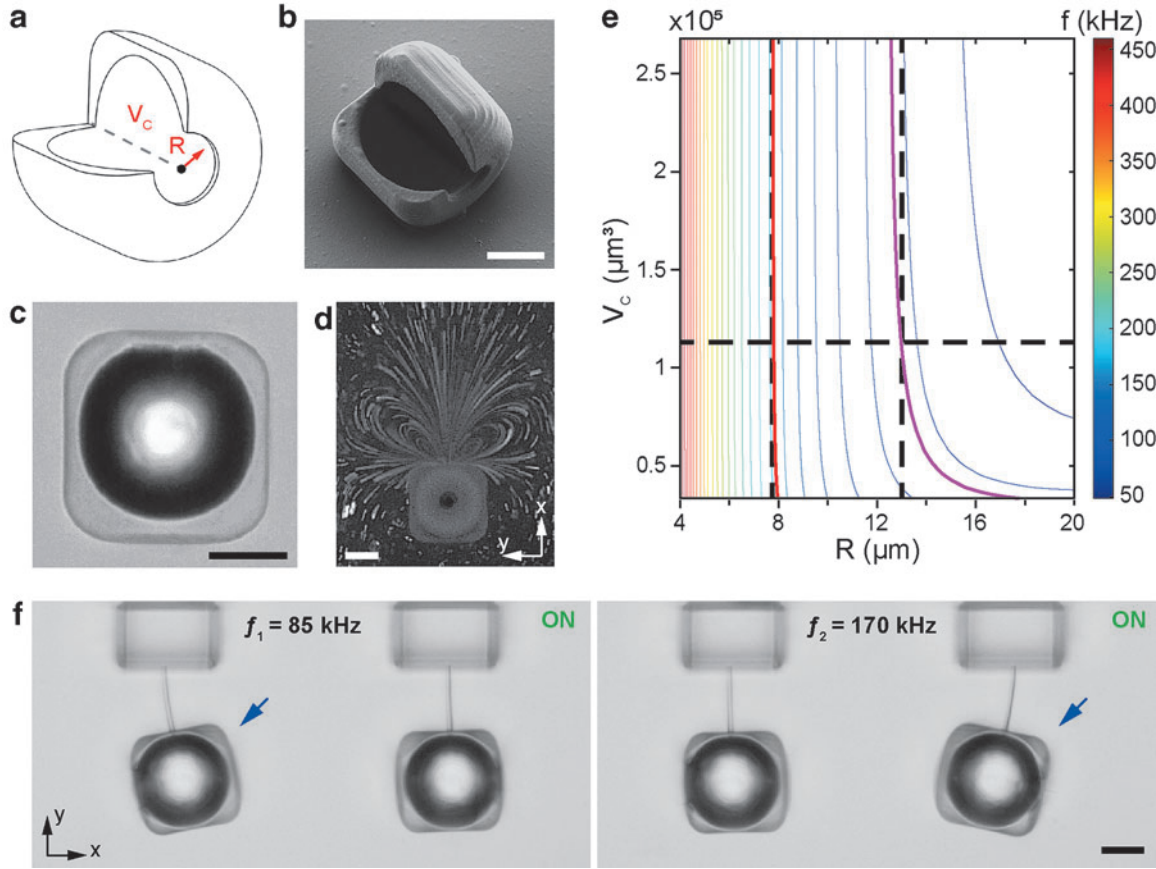


FIG. 2. Design, fabrication, and operation of acoustic actuator modules. (a) The natural oscillation frequency of entrapped microbubbles were set by tuning the volume of the cavity, V_c , and the radius of the orifice, R . (b) Scanning electron microscopy image of a partially printed actuator module shows the cavity and the orifice. (c) Brightfield images of an actuator module when the air bubble is entrapped inside the cavity. (d) Streamlines around an acoustic module are visualized using fluorescent tracer particles. (e) A computed contour plot showing the dependence of the entrapped microbubble natural frequency on the orifice size (R) and cavity volume (V_c). The black dashed lines indicate the volume and radii that correspond to the selected geometric parameters. The red and magenta curves denote the operating frequencies of 170 and 85 kHz, respectively. (f) Frequency-selective powering of multiple actuator modules. The first natural frequencies of the two modules are set by prescribing different orifice sizes. The blue arrow points to the actuator module that is activated at the specified frequencies, f_1 and f_2 . Scale bars, 20 μm .

extended a previously published model⁵³ to accommodate multiple orifices on the same cavity, incorporate all the possible mode shapes, and consider the geometry adjacent to the orifice. We derived the model by formulating the potential and kinetic energy in the system. The contribution to the kinetic energy comes from the fluid motion while the gas compressibility and interface deformation determine the potential energy. The acoustic wavelength is much larger than the capsule's largest dimension for the frequencies studied in this work. Thus, the instantaneous pressure in the gas can be considered uniform and, as a result, the interior shape of the capsule has a negligible effect. The spherical shape was chosen to maximize the gas volume, increase the bubble's stability, and simplify the printing procedure.

We recorded the power spectrum of the ultrasound transducer using a hydrophone to determine the frequency bands at which the actuators could be effectively powered (Supplementary Fig. S2). Using our model, we designed the geometry (i.e., volume and orifice radii) so that the first natural frequencies of the entrapped bubbles are within these bands

(Fig. 2e). For the chosen parameters, variations in the bubble orifice radius, R , have a greater influence on the natural frequency than the internal volume, V_c , because R influences both the potential and kinetic energy of the system. We printed two capsules with orifice radii of 7.75 and 13 μm , respectively (Supplementary Table S1). Entrained bubbles were actuated selectively at their estimated natural frequencies of either 85 or 170 kHz, which led to a sequential deformation of the beams (Fig. 2f and Supplementary Movie S2).

Actuators with orifices close to the substrate are not ideal for the quantification of forces because the entrapped bubbles may interact with the substrate's surface.^{44,45} To minimize such perturbations, we printed the beams vertically, raising the actuator modules 50 μm above the substrate (Fig. 3a). Laser scanning confocal microscope images of fluorescently labeled samples verified that the structures were printed according to the CAD design (Supplementary Fig. S3). In this configuration, the beam bending could be followed from the actuator's in-plane displacement (Fig. 3b), which increased quadratically with the input voltage (Fig. 3c). The bending

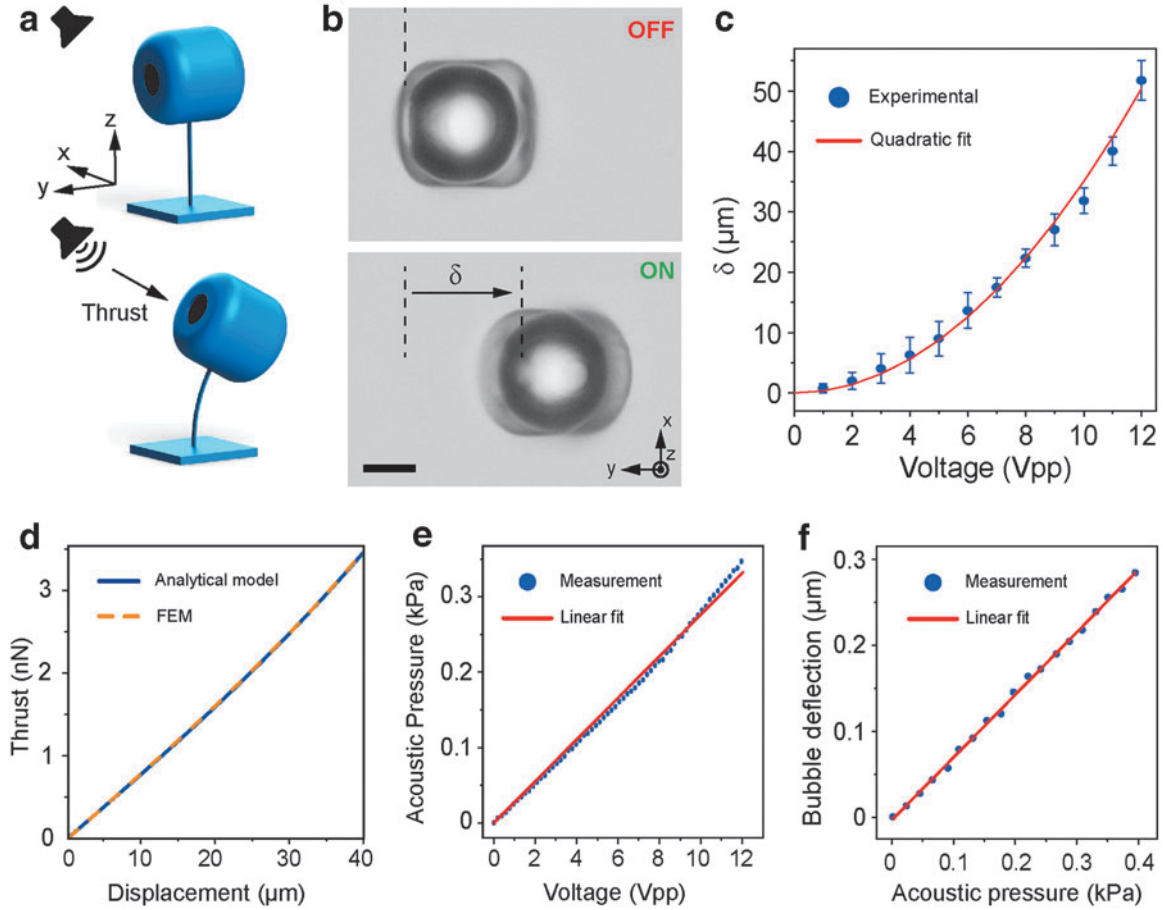


FIG. 3. Mechanical characterization of the actuator module and the pressure field. **(a)** Schematic illustration of the bending of a flexible cantilever beam that is printed vertically to minimize the interactions of the actuator module with the bottom surface. **(b)** Brightfield images showing the displacement of the actuator module, which is denoted as δ . δ is used to measure the deflection of the beam. Scale bar, $20\ \mu\text{m}$. **(c)** The displacement increases quadratically with the voltage applied to the acoustic transducer. **(d)** The thrust calculated using a linear analytical model and a FEM model are in excellent agreement. **(e)** The acoustic pressure increases linearly with the voltage applied to the transducer. Pressure measurements were performed using a hydrophone. **(f)** The deflection of the entrapped bubble measured at the center of the orifice linearly increases with the acoustic pressure. The deflection was measured using a laser vibrometer. FEM, finite element method.

modulus was calculated from the material's Young's modulus, $E=13\ \text{MPa}$,⁴⁷ and the dimensions of the beam were measured using electron microscopy (Supplementary Fig. S3). The generated force was then estimated using linear beam theory (Supplementary Note S2).

Although the linear theory was used, the displacement is a nonlinear function of the applied force because the part of the beam corresponding to the location of the actuator was taken as rigid (Supplementary Fig. S10). The tip displacement, δ , is given as:

$$\delta = \frac{LP}{6EI} \left[L(3l + 2L) + \frac{6l(2l + L)}{\sqrt{4 + \frac{L^2(2l + L)^2 P^2}{E^2 I^2}}} \right] \quad (1)$$

where L is the length of the beam, l is the length of half the actuator, E is Young's modulus, I is the second moment of inertia of the cross-section and P is the applied force. Nonlinear finite element method (FEM) simulations (i.e., large deforma-

tions) using linear elastic material ($E=13\ \text{MPa}$ and Poisson's ratio is taken as 0.45) were in perfect agreement with the analytical model, thus confirming that the linearity assumption was acceptable for the given range of deflections (Fig. 3d). The analytical model was used to calculate the total force acting on a deforming beam from the recorded deflection.

We observed a linear relationship between the voltage applied to the transducer and the resultant acoustic pressure measured by a hydrophone (Fig. 3e), as predicted by the theory.⁵⁴ The acoustic energy density in the workspace quadratically increases with increasing pressure,⁵⁵ and so does the streaming velocity around the bubble.⁴⁴ Sequentially increasing the input voltage resulted in a new configuration within milliseconds. Furthermore, when the input voltage was turned off, the beam immediately returned to its original position, confirming that the actuation was in the elastic range. We characterized the oscillation amplitude at the bubble's first natural frequency using a custom-built experimental platform (Supplementary Fig. S4). The data showed that the deflection amplitude at the air-fluid interface increases linearly for the range of pressure we applied (Fig. 3f).

An actuator module with multiple DOF would drastically increase the dexterity and form factor of printed structures. We postulated that a capsule, which contains multiple orifices of different sizes, would serve this purpose. To test this idea, we printed an actuator module in the shape of an equilateral triangular prism with three orifices, one at the center of each face (Fig. 4a). The actuator module was connected atop a 50- μm -long and 2- μm -diameter cantilever beam. The sizes of the orifices (15, 9.5, and 7 μm) were chosen in a way that corresponding natural frequencies were well spaced and within the effective range of the transducer (Fig. 4b). Simulation results have shown that primarily one interface is deformed at each mode (Fig. 4c).

We excited the system at multiple frequencies simultaneously to control the position. The force is unidirectional,

therefore, at least three frequencies are required to fully control the 2D position. Ideally, these frequencies are the ones where the largest displacement is obtained, which are expected to be the bubble's natural frequencies. However, the transducer has its own dynamical response, and the input pressure varies with the excitation frequency (Supplementary Fig. S2). We addressed this issue by experimentally calibrating the response of the system.

We recorded the actuator motion while sweeping the frequency from 40 to 160 kHz at a constant input voltage. Using a subpixel resolution image processing algorithm,⁵⁶ we extracted the planar position of the module (Supplementary Fig. S5a). We then selected three frequencies where the largest deflections in different axes were recorded. Figure 4d shows the undeformed and deformed states of the system at

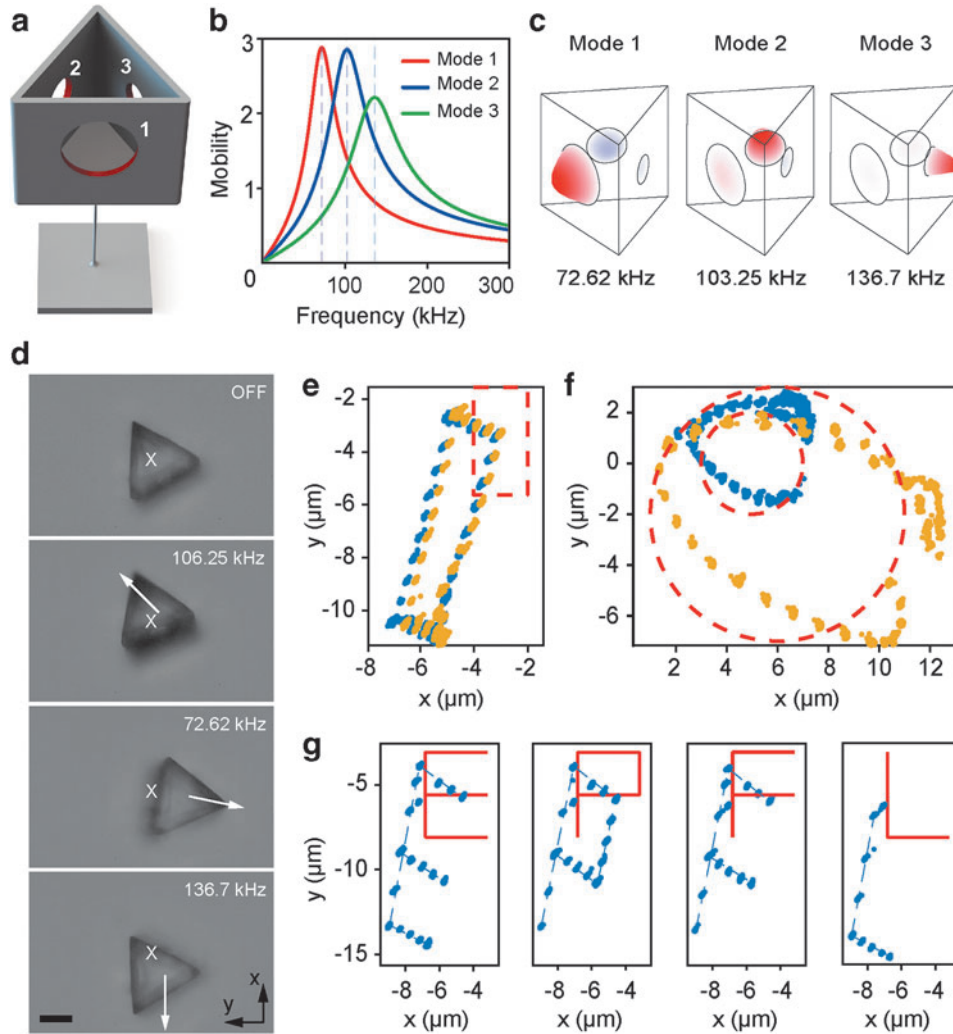


FIG. 4. Design, calibration, and control for multi DOF motion. (a) An illustration of the actuator module with multiple orifices. The ceiling is removed for visualization. The different orifices are numbered starting from the largest to the smallest. The radii are 15, 9.5, and 7.5 μm , respectively. (b) A modal mobility plot, showing the first three modes of the system excited with uniform pressure. *Dashed lines* highlight the natural frequencies. (c) An illustration of the first three normal vibration modes. Deformation of the interfaces is scaled according to the amplitude of calculated deflection. (d) Brightfield images of a device showing the deflection as a response to excitation at the chosen frequencies. (e) A system is driven with the same signal twice to follow a rectangular trajectory. The rectangle in *red dashed lines* shows the desired trajectory. (f) A system is driven to follow two circular trajectories of different sizes. *Circles in red dashed lines* show the desired trajectories. (g) An actuator module moving along the letters of EPFL. Data points are shown by *blue dots* and prescribed trajectories are shown by *red continuous lines*. Scale bar, 20 μm . DOF, degrees of freedom; EPFL, Ecole Polytechnique Fédérale de Lausanne.

the chosen frequencies. Next, we measured the actuator's deflection at each frequency and built the vectors spanning the planar displacement field. We implemented an open-loop controller that leverages the superposition principle and excites the system with a signal comprising three harmonic terms, which correspond to the aforementioned vectors. We controlled two DOF with three forces, thus, there are infinite combinations. We solved a constrained linear least-squares problem,⁵⁷ where we minimized the voltage signal amplitude.

We performed a series of experiments to evaluate the control strategy. First, we programmed a calibrated device to repeatedly follow a rectangular trajectory, slightly offset from the origin where we had better control over the motion (Fig. 4e). Second, we programmed several circular trajectories with different radii and offsets (Supplementary Movie S3). The position error increased with the distance from the origin (Fig. 4f). Third, we used the calibration parameters of one device to control another with the same design (Supplementary Fig. S5b). The trajectories of the two devices were close, suggesting that calibration might be performed once and used repeatedly for different devices. As a final demonstration, we designed four trajectories prescribing the initials Ecole Polytechnique Fédérale de Lausanne to show that control was not limited to specific geometries (Fig. 4g).

Acoustically excited bubbles interact with each other through the surrounding fluid when they reside in close proximity. The total force acting on a bubble is the result of the exciting primary pressure field, and higher-order fields emanating from neighboring bubbles that also act as acoustic sources.^{38,58} The distances between bubbles are significantly smaller than the acoustic wavelength in all our prototypes. Therefore, we can assume that the acoustic radiation forces caused by the primary field do not affect the relative displacement of the actuators. The secondary forces that act on the coupled actuators are thrust, drag-induced acoustic streaming, and secondary acoustic radiation force (also known as secondary acoustic radiation force or secondary Bjerknes force). Identical bubbles are expected to generate the same acoustic streaming; thus, the generated thrust would push the bubbles away from each other. On the other hand, the magnitude of the acoustic radiation force, which primarily acts to pull the bubbles toward each other, depends on the distance between them.^{38,58}

The total force, \mathbf{F}_B , acting on an untethered bubble is

$$\mathbf{F}_B = \mathbf{F}_R + \mathbf{F}_{AS} + \mathbf{F}_d \quad (2)$$

where \mathbf{F}_R denotes the acoustic radiation force, \mathbf{F}_{AS} denotes thrust generated by streaming, and \mathbf{F}_d is the drag force acting on a bubble due to the streaming generated by the adjacent bubble. In the following analysis, we simplify the kinematics by assuming that actuators move along a virtual line connecting their centers.

To quantify the total force generated by interacting bubbles, we printed two adjacent cantilever beams with identical actuators that were faced toward each other (Supplementary Table S1). The initial distance between the actuators, d_i , was systematically varied to study the effect of spacing. At equilibrium, $|\mathbf{F}_B|$ in Equation (2) equals the elastic force applied by the cantilever beam, denoted by P in Equation (1). We observed two distinct regimes in the dynamics of the coupled actuators (Supplementary Movie S4). When the initial dis-

tance between the actuators was smaller than a critical distance, d_c , the radiation forces dominated the thrust generated by acoustic streaming (Fig. 5a). For the given actuator design, this critical distance was $50 \mu\text{m}$ (i.e., $d_c = 50 \mu\text{m}$). As a result, the beams bent toward each other until the bubbles made contact (Fig. 5b). With increasing d_i , the magnitude of the acoustic radiation force decreased, emphasizing the contribution of streaming forces (Fig. 5c). For $d_i > d_c$, the sign of the total force switched, where the beams started to move away from each other (Fig. 5d).

Figure 5e summarizes the nonlinear responses of coupled actuators with respect to the initial distance and the input voltage. The further away the actuators were from each other at rest, the more the beam deflection resembled that of the isolated single beam (Fig. 3c). Based on this empirical observation, we hypothesized that the dynamics could be captured by an analytical model where all forces are proportional to the input voltage squared.⁵⁹ We assumed that \mathbf{F}_d did not depend on the distance between the actuators, therefore $|\mathbf{F}_{AS}| = |\mathbf{F}_d|$ at all times. This assumption is reasonable as the distance between the bubbles was always comparable to the bubble size, which was significantly shorter than the acoustic wavelength.

We also assumed that \mathbf{F}_R inversely depends on the distance squared.^{38,58} The force balance equation, Equation (2), is then rewritten as:

$$\mathbf{F}_B = (2\gamma - \alpha d^{-2}) V^2 \quad (3)$$

where $F_B > 0$ indicates bubble repulsion,³⁷ α and γ are functions of the excitation frequency and geometry, and d is the distance between the bubbles' vibrating surface. We fitted $\alpha = 174.5 \text{ nN V}^{-2} \mu\text{m}^{-2}$, and $\gamma = 0.027 \text{ nN V}^{-2}$ at 125 kHz to the empirical data shown in Figure 5e. The model could capture the dynamics represented in the experimental data (Supplementary Fig. S6). This analytical model has been used to design the prototypes presented in the rest of the article.

Our results have shown that radiation forces between identical actuator modules do not change direction for a given spacing. Actuators with different orifice sizes displayed more complex interactions. We discovered that depending on the excitation frequency, actuators with the same initial distance attracted or repelled each other. An analogous phenomenon was observed between acoustically excited free-floating spherical bubbles with different radii.^{38,58}

Different bubbles oscillate with a different amplitude and phase for the same impinging pressure wave (Fig. 5f). The relative oscillation phase dictates the direction of the radiation force. When the bubbles oscillate in a relative phase of less than a quarter of a period, the force is attractive, but if the phase differs by more than a quarter but less than three-quarters of a period, the force is repulsive. Therefore, identical bubbles tend to attract each other, and nonidentical bubbles can either attract or repel each other, depending on the excitation frequency (Fig. 5g). In our experiments, actuator modules with cavity radii of 25 and $17.5 \mu\text{m}$ and orifice radii of $10 \mu\text{m}$, attracted or repelled one another at 85 and 125 kHz, respectively (Fig. 5h and Supplementary Movie S5).

We designed a flextensional mechanism that leverages this frequency-dependent behavior to manifest multiple distinct deformation patterns on the same system (Supplementary Fig. S7 and Supplementary Movie S6). Both couples of arms

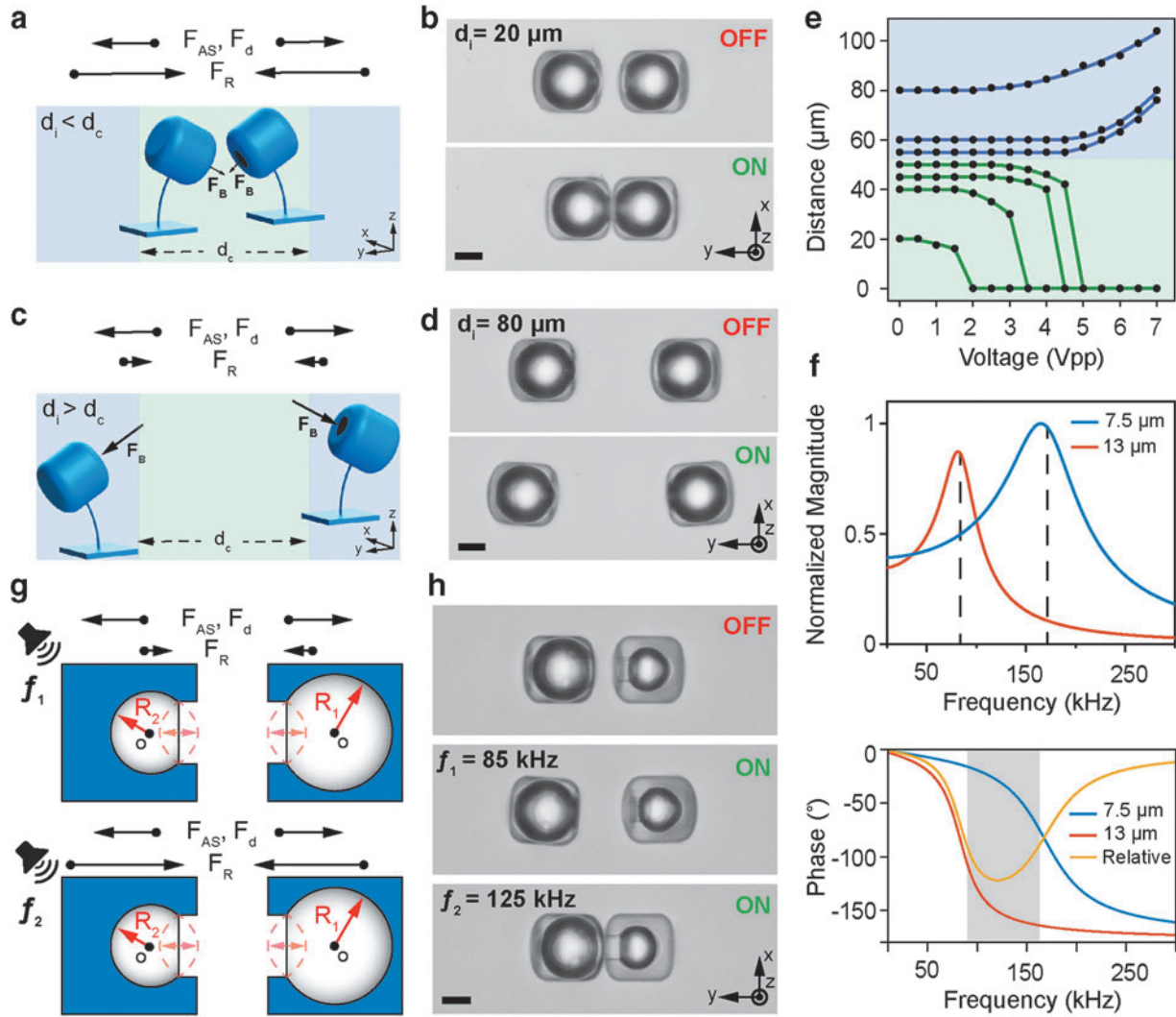


FIG. 5. Characterization of acoustic radiation forces between two actuator modules. **(a)** An illustration showing the relative magnitude of the three forces acting on the actuator module; drag force (\mathbf{F}_d), acoustic streaming force (\mathbf{F}_{AS}), and acoustic radiation force (\mathbf{F}_R) for the case where the initial distance (d_i) between the actuator modules is shorter than the critical distance (d_c). In this case, \mathbf{F}_R is larger than the sum of the other two forces. **(b)** Representative microscope images from an experiment where the actuator modules were attracted to each other and, as a result, the beams bent toward each other. **(c)** An illustration showing the relative magnitude of the three forces acting on the actuator module for the case where d_i is longer than d_c . In this case, \mathbf{F}_{AS} and \mathbf{F}_d dominate the radiation force. **(d)** Microscope images from an experiment where the actuator modules moved away from each other and, as a result, the beams bent in opposite directions. **(e)** The equilibrium distance between acoustically actuated beams as a function of input voltage. The beams were printed with different spacing. In all the experiments, the frequency was tuned to 125 kHz. **(f)** The theoretical bode plot. The *top panel* depicts the normalized oscillation magnitude, where the natural frequencies are highlighted by *black dashed lines*. The *blue* and *orange curves* in the *lower panel* show the phase response of the small and big bubbles, respectively. The *yellow curve* depicts the phase difference. In the *gray region*, the phase difference results in a repulsive force while in the *white regions* the interbubble forces are attractive. **(g)** A schematics showing the frequency-dependent motion of actuator modules with different cavity sizes. The in-phase and out-of-phase vibrations of the entrapped bubble determine the magnitude of the radiation forces. **(h)** Representative brightfield images showing the frequency-dependent deformation of coupled beams. Scale bars, 20 μm .

simultaneously closed at one frequency, and one couple opened while the other closed at another frequency. The frequencies at which the arms would open or close were determined by the relative phase of oscillations, which was modified by capsule geometry. Both operation modes were independent of the input signal amplitude, therefore, the angle between the arms could be tuned with the applied voltage.

So far, we focused on a paradigm where actuator modules were patterned on different structures. In this arrangement, a rapid increase in radiation forces with decreasing distance limits the range of motion that the actuators can generate. To extend the interval at which the structure bends in a graded fashion, we constrained the actuators' motion. To this end, we connected two actuators with a truss so that they were not

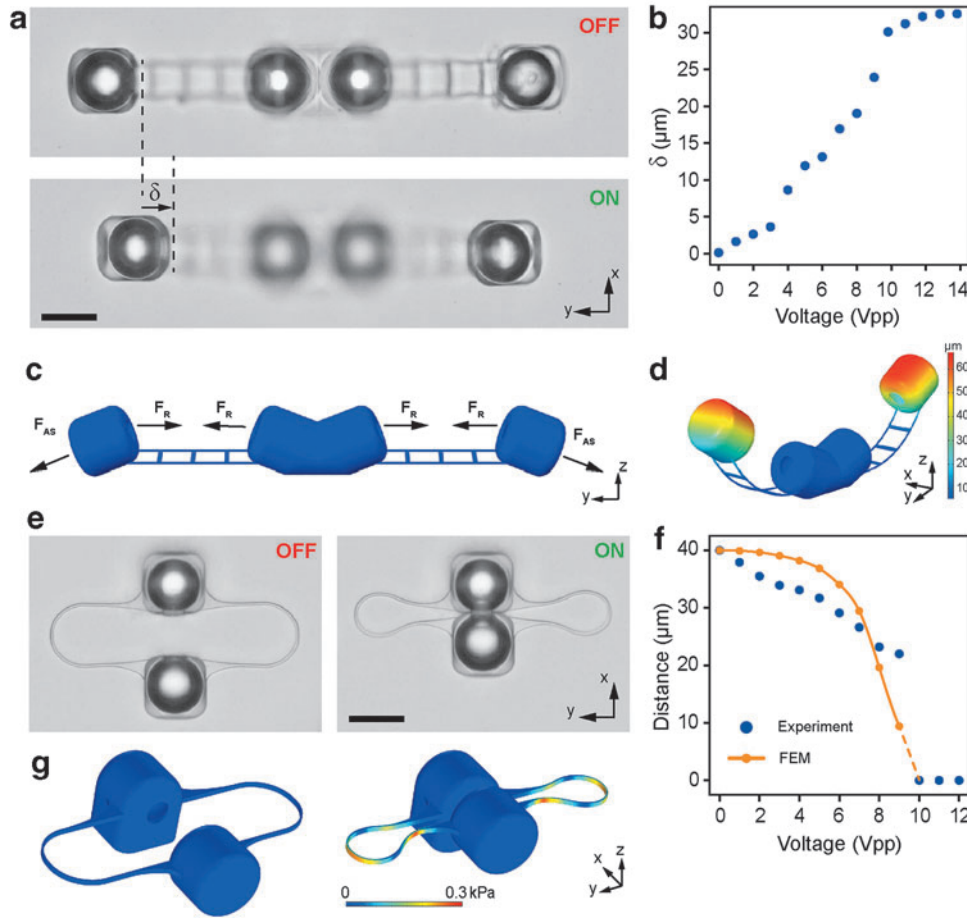


FIG. 6. Mechanical programming of soft micromachines. **(a)** Out-of-plane deformation mechanism. Two pairs of identical actuator modules are printed on both arms. The displacement, δ , is used to measure the bending of the arms. **(b)** δ Increases monotonically with increasing voltage until a threshold at which the deformation ceases. The radiation forces generated by the entrapped bubbles are insufficient to bend the structure further. The actuator modules are constrained in their motion so that they do not snap with each other. **(c)** A CAD model and free body diagram of the out-of-plane deformation mechanism. **(d)** The deformed configuration of the out-of-plane mechanism as computed by the FEM model. **(e)** A linear microactuator constructed with a flexible spring mechanism. The top actuator module is fixed to the ground while the bottom one is free to move. The motion of the bottom actuator module is constrained in the y -axis by the spring mechanism. **(f)** The distance between the actuator modules gradually decreases with the input voltage, where beyond $20 \mu\text{m}$ increasing the voltage further abruptly closes the gap. Simulation results closely match the experimental data. **(g)** A 3D FEM model of the machine showing the stresses acting on the mechanism. The same model is used to calculate the stiffness of the spring. Scale bars, $50 \mu\text{m}$.

allowed to come very close to each other (Fig. 6a). As expected, the arms progressively bent out of plane for a large range of input voltage (Supplementary Movie S7). To report the deformation, we recorded the displacement of the actuators along the y -axis (Fig. 6b). Although the arms bent under the dominant radiation forces, the displacement curve did not follow the highly nonlinear trend presented in Figure 5e. We built a FEM model of the mechanism based on the CAD design and the material properties (Fig. 6c, d). The radiation force magnitude and its direction are expected to change as the arms bend due to the relative position of the bubbles.

We simplified the model by assuming that the radiation force always acted to pull the actuators toward each other, and its magnitude was proportional to the thrust. We took the thrust calculated for a single actuator module (Fig. 3) as input and estimated the acoustic radiation force for the applied voltage values by fitting the empirical data shown in

Figure 6b. In this study, the acoustic radiation force was taken as $\mathbf{F}_R = -\beta V^2 d^{-2}$ following Equation (2), where β was estimated as $745.6 \text{ nN V}^{-2} \mu\text{m}^{-2}$ (Supplementary Note S3 and Supplementary Fig. S11). In the experiments, at relatively high voltage values, further increment did not cause further deformation (Fig. 6b). The experimentally observed plateau may be due to the drag force applied to the moving actuators by the anchored ones.

The out-of-axis bending is a classic example for unimorph actuators where we control the angular displacement. By simply connecting a microbubble pair with an ultraflexible spring mechanism, we developed a linear microactuator (Fig. 6e). Acoustic forces were primarily uniaxial and, as expected, we did not observe out-of-axis deflection during operation (Supplementary Movie S8). Attractive radiation forces between the two microbubbles caused the gap to narrow. The deflection of the spring followed an almost linear trend with respect to

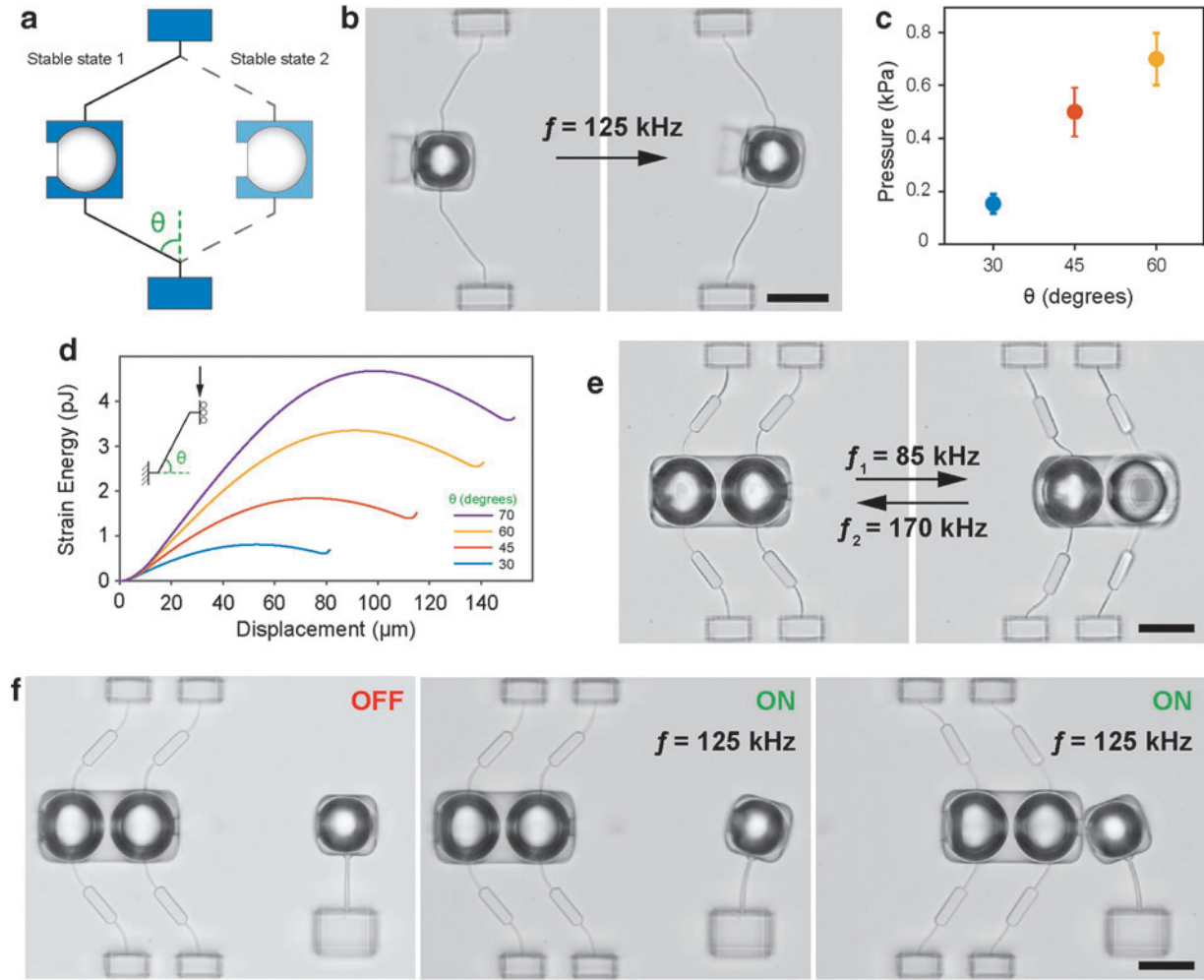


FIG. 7. Mechanical reprogramming of soft micromachines through elastic instabilities. (a) The design of a bistable mechanism with a snap through. The inclination angle, θ , is modulated to construct mechanisms with varying energy barriers. (b) Representative microscope images showing the switching of a bistable mechanism from one stable state to another upon acoustic excitation. The mechanism stays indefinitely in both stable states unless it is excited to switch. (c) The acoustic pressure required to pass the energy barrier and switch the mechanism for prototypes with varying θ . (d) The energy landscape of bistable mechanisms with different θ . (e) Reversible actuation of bistable mechanisms. Two actuator modules with identical cavity sizes and distinct orifice sizes are connected on the same unit for frequency selective actuation in opposite directions. (f) A bistable mechanism was used as a control module. A third separate actuator module deformed a cantilever beam in the clockwise direction when the control module is kept at one stable state. Switching the control module to the left completely changes the force balance on the third actuator module. The radiation forces generated between the control module and the third actuator module reversed the motion and deformed the beam in the counterclockwise direction. Scale bars, $50 \mu\text{m}$.

applied voltage until the bubbles were $20 \mu\text{m}$ apart, at which point the radiation forces overcame the structural stiffness leading to a fast closure of the mechanism (Fig. 6f), similar to the pull-in instability observed in microelectromechanical systems devices.⁶⁰

When the excitation signal was turned off, the acoustic forces vanished, and the actuator returned to its initial position. We calculated the magnitude of forces that correspond to the input voltage using Equation (3) and applied these forces to an FEM model. The model captured the behavior of the experimentally recorded spring deflection, verifying that we have a reliable way of calculating forces generated by the acoustic actuator modules (Fig. 6f, g). We calculated the stiffness of the spring as $0.7563 \text{ nN}/\mu\text{m}$ by computing the derivative of the displacement with respect to the total force (Supplementary Fig. S8).

Constrained elastic beams can exhibit complex mechanical responses depending on the geometry, degree of confinement, and boundary conditions. Previous work has shown that such mechanisms instantiate embodied logic and programmable functionality in soft machines.^{19,33,61,62} We designed beams to present a snap-through instability so that application of a relatively small thrust would be sufficient to cross the energy barrier and trigger rapid and large deformation toward a second stable configuration. Key geometric parameters for the beam design are the inclination angle of the beam, θ , and the slenderness ratio, w/L , where w and L denote the width and length of the beam, respectively (Fig. 7a). The mechanism was driven by a single actuator module that operated in acoustic streaming mode (Fig. 7b). The modules stayed indefinitely in both stable states, and the thrust generated by the actuator module was high enough to pass the energy barrier.

For a fixed beam length and cross-sectional profile, as θ increases, the input pressure required to switch the mechanism state is expected to increase while the deformed position becomes more stable.²⁰ We fabricated three different prototypes that only differ in inclination angle ($\theta = 30^\circ$, 45° , and 60°) to validate the theoretical predictions. We observed a monotonic increase in the pressure at which the beam managed to switch states (Fig. 7c).

We used a 2D FEM model to obtain the double-well potential energy landscape for the same design parameters (Fig. 7d). The simulation results showed that the strain energy quadruples when θ is increased from 30° to 70° , and the module displacement doubles. We calculated the force required to switch the mechanism at different θ from the empirical data using Equation (3), where we only considered the thrust generated by a single actuator module (i.e., $|\mathbf{F}_B| = 0.027V^2$). Comparing these values with the simulated force showed that the switching occurred at lower levels than predicted (Supplementary Table S2). The rationale behind this discrepancy is that the actuator module did not move along a straight line as simulated, and, instead, moved in 3D by following a more favorable energy landscape.

We harnessed frequency-selective thrust generation to realize reversible actuation for the bistable mechanism (Fig. 7e). We kept the bubble size constant and tuned the actuators' orifice size to be able to activate them at distinct frequencies, 85 and 170 kHz (Fig. 2e). Connecting two actuator modules with a single beam to the anchor point proved to be undesirable. To stabilize the structure and ensure reliable operation, we extended the mechanism by adding support structures. The resulting mechanism could be switched repeatedly at the same amplitude and excitation frequency (Supplementary Movie S9).

As a final demonstration, we programmed the motion of a continuously bending cantilever beam using an actuated bistable mechanism, which we refer to as the control module (Fig. 7f-left). Here, triggering the control module changes the direction of bending by introducing radiation forces to a system otherwise driven solely by acoustic streaming (Supplementary Movie S10). To trigger the controller and actuate the beam at different frequencies, we engineered capsules with different geometries. At 125 kHz, the beam bent clockwise while the control module stayed idle (Fig. 7f-middle). Exciting the system at 85 kHz activated the bubble located on the left of the control module, moving the right one closer to the actuator connected to the beam. The control module stayed in this stable state when the system was turned off, as expected. Then, exciting the system again at 125 kHz bent the beam counterclockwise due to the attractive radiation forces generated between the two neighboring bubbles (Fig. 7f-right).

In this prototype, the control module must be reset manually because the radiation forces are stronger than the thrust. However, by tuning the bubbles' geometry, we can introduce a third frequency at which the control module would be reset.

Conclusions

We introduced a suite of mechanical microsystems with relatively basic design yet complex motion. Precise control over geometric parameters facilitated detailed analysis of for-

ces and fluid-structure interactions. We made two important discoveries. First, we showed that a single bubble can provide multiple-DOF motion along prescribed trajectories with high fidelity through the application of frequency- and amplitude-modulated acoustic signals. Second, as a result of higher-order interactions, forces between oscillating bubbles emerge, and their amplitude and direction can be programmed by tuning the excitation frequency. The realization of the former required printing of capsules with multiple orifices at different sizes, a calibration process, and dynamic control.

Direct laser writing has been used to develop wireless soft microactuators powered by magnetic fields⁶³ and photo-thermal effects.^{64,65} Acoustic actuation is appealing for *in vivo* biomedical applications, specifically to remotely steer ultraflexible microcatheters⁶⁶ and control the release of biologics from miniaturized wireless implants.⁶⁷ Ultrasound is minimally invasive, acoustic microactuators are compatible with magnetic resonance imaging, generating acoustic waves does not require sophisticated and expensive equipment, and the whole device is fully biodegradable.

We developed an open-loop control scheme that drives a mechanical system to follow prescribed trajectories by applying a complex signal, based on the model and calibration. The position errors between the programmed and executed motion are not negligible, which may stem from multiple sources. We assumed that the 3D printed cantilever beam has isotropic stiffness. However, the material stiffness depends on the degree of polymerization, which might show spatial variations along the vertical axis. Moreover, the controller assumes small deflections although the beam deflected beyond the limit defined by the theoretical linear model. Finally, at relatively large deflections, the beam started to tilt out-of-plane and rotate around its axis while we only considered in-plane translation.

We focused our attention on geometric arrangements of entrapped bubbles, as a means to program the soft robotic system. Leveraging frequency-selective bubble excitation, we could operate systems in different modes at different frequencies. Considering the interactions among neighboring actuators would advance the programming framework. An actuator may be attracted to other actuators from multiple directions, realizing a sophisticated motion that highly depends on the excitation frequency and time-varying spacing among bubbles. We have also incorporated acoustically actuated bistable mechanisms as onboard control units to introduce the capability to operate in different modes under the same input signal.

This last functionality represents the first step toward reconfigurable mechanical systems that operate analogously to mechatronic systems. To this end, reversible switching of several bistable structures will be instrumental. Moving forward, bistable beams could be replaced by 3D architected materials that display sensing, pattern analysis, and multistability.^{68–70} The fabrication of such complex structures is feasible with two-photon lithography, and local actuation initiated by entrapped bubbles will reveal unprecedented reconfigurability and multifunctionality.

Acknowledgments

The authors thank Dr. Guillermo Villanueva for generously providing the vibrometer, Dr. Pedro Reis for fruitful discussions, and Furkan Ayhan for his assistance with electron microscopy imaging.

Author Disclosure Statement

No competing financial interests exist.

Funding Information

This work was supported by the European Research Council (ERC) under the European Union's Horizon 2020 research and innovation program (Grant agreement No. 714609), and the Marie Skłodowska-Curie Actions Post-doctoral Fellowship (Grant agreement No. 101022448).

Supplementary Material

Supplementary Note S1
 Supplementary Note S2
 Supplementary Note S3
 Supplementary Table S1
 Supplementary Table S2
 Supplementary Figure S1
 Supplementary Figure S2
 Supplementary Figure S3
 Supplementary Figure S4
 Supplementary Figure S5
 Supplementary Figure S6
 Supplementary Figure S7
 Supplementary Figure S8
 Supplementary Figure S9
 Supplementary Figure S10
 Supplementary Figure S11
 Supplementary Movie S1
 Supplementary Movie S2
 Supplementary Movie S3
 Supplementary Movie S4
 Supplementary Movie S5
 Supplementary Movie S6
 Supplementary Movie S7
 Supplementary Movie S8
 Supplementary Movie S9
 Supplementary Movie S10

References

1. Erb RM, Sander JS, Grisch R, *et al.* Self-shaping composites with programmable bioinspired microstructures. *Nat Commun* 2013;4:1712.
2. Jochum FD, Theato P. Temperature- and light-responsive smart polymer materials. *Chem Soc Rev* 2013;42:7468–7483.
3. Stuart MAC, Huck WTS, Genzer J, *et al.* Emerging applications of stimuli-responsive polymer materials. *Nat Mater* 2010;9:101–113.
4. Wu S, Hu W, Ze Q, *et al.* Multifunctional magnetic soft composites: A review. *Multifunct Mater* 2020;3:042003.
5. Huang HW, Uslu FE, Katsamba P, *et al.* Adaptive locomotion of artificial microswimmers. *Sci Adv* 2019;5:1–8.
6. Nelson BJ, Kaliakatsos IK, Abbott JJ. Microrobots for minimally invasive medicine. *Annu Rev Biomed Eng* 2010;12:55–85.
7. Fusco S, Sakar MS, Kennedy S, *et al.* An integrated microrobotic platform for on-demand, targeted therapeutic interventions. *Adv Mater* 2014;26:952–957.
8. Yang G-Z, Bellingham J, Dupont PE, *et al.* The grand challenges of science robotics. *Sci Robot* 2018;3:eaar7650.
9. Cianchetti M, Laschi C, Menciassi A, *et al.* Biomedical applications of soft robotics. *Nat Rev Mater* 2018;3:143–153.
10. Palagi S, Fischer P. Bioinspired microrobots. *Nat Rev Mater* 2018;3:113–124.
11. Soto F, Wang J, Ahmed R, *et al.* Medical micro/nanorobots in precision medicine. *Adv Sci* 2020;7:2002203.
12. Soto F, Karshalev E, Zhang F, *et al.* Smart materials for microrobots. *Chem Rev* 2022;122:5365–5403.
13. Dolev A, Kaynak M, Sakar MS. On-board mechanical control systems for untethered microrobots. *Adv Intell Syst* 2021;3:2000233.
14. Lum GZ, Ye Z, Dong X, *et al.* Shape-programmable magnetic soft matter. *Proc Natl Acad Sci U S A* 2016;113:E6007–E6015.
15. Hu W, Lum GZ, Mastrangeli M, *et al.* Small-scale soft-bodied robot with multimodal locomotion. *Nature* 2018;554:81–85.
16. Kim Y, Yuk H, Zhao R, *et al.* Printing ferromagnetic domains for untethered fast-transforming soft materials. *Nature* 2018;558:274–279.
17. Palagi S, Mark AG, Reigh SY, *et al.* Structured light enables biomimetic swimming and versatile locomotion of photoresponsive soft microrobots. *Nat Mater* 2016;15:647–653.
18. Rogó̄z M, Zeng H, Xuan C, *et al.* Light-driven soft robot mimics caterpillar locomotion in natural scale. *Adv Opt Mater* 2016;4:1689–1694.
19. Song Y, Panas RM, Chizari S, *et al.* Additively manufacturable micro-mechanical logic gates. *Nat Commun* 2019;10:882.
20. Jiang Y, Korpas LM, Raney JR. Bifurcation-based embodied logic and autonomous actuation. *Nat Commun* 2019;10:1–10.
21. Raney JR, Nadkarni N, Daraio C, *et al.* Stable propagation of mechanical signals in soft media using stored elastic energy. *Proc Natl Acad Sci* 2016;113:9722–9727.
22. Bertoldi K, Vitelli V, Christensen J, *et al.* Flexible mechanical metamaterials. *Nat Rev Mater* 2017;2:17066.
23. Treml B, Gillman A, Buskohl P, *et al.* Origami mechanologic. *Proc Natl Acad Sci U S A* 2018;115:6916–6921.
24. Preston DJ, Rothmund P, Jiang HJ, *et al.* Digital logic for soft devices. *Proc Natl Acad Sci U S A* 2019;116:7750–7759.
25. Kadic M, Milton GW, van Hecke M, *et al.* 3D metamaterials. *Nat Rev Phys* 2019;1:198–210.
26. Pal A, Restrepo V, Goswami D, *et al.* Exploiting mechanical instabilities in soft robotics: Control, sensing, and actuation. *Adv Mater* 2021;33:2006939.
27. Yasuda H, Buskohl PR, Gillman A, *et al.* Mechanical computing. *Nature* 2021;598:39–48.
28. El Helou C, Buskohl PR, Tabor CE, *et al.* Digital logic gates in soft, conductive mechanical metamaterials. *Nat Commun* 2021;12:1633.
29. Meng Z, Chen W, Mei T, *et al.* Bistability-based foldable origami mechanical logic gates. *Extrem Mech Lett* 2021;43:101180.
30. Forterre Y, Skotheim JM, Dumais J, *et al.* How the venus flytrap snaps. *Nature* 2005;433:421–425.
31. Son K, Guasto JS, Stocker R. Bacteria can exploit a flagellar buckling instability to change direction. *Nat Phys* 2013;9:494–498.
32. Kühn MJ, Schmidt FK, Eckhardt B, *et al.* Bacteria exploit a polymorphic instability of the flagellar filament to escape

- from traps. *Proc Natl Acad Sci U S A* 2017;114:6340–6345.
33. Rafsanjani A, Bertoldi K, Studart AR. Programming soft robots with flexible mechanical metamaterials. *Sci Robot* 2019;4:eaav7874.
 34. Chen T, Bilal OR, Shea K, *et al.* Harnessing bistability for directional propulsion of soft, untethered robots. *Proc Natl Acad Sci U S A* 2018;115:5698–5702.
 35. Drotman D, Jadhav S, Sharp D, *et al.* Electronics-free pneumatic circuits for controlling soft-legged robots. *Sci Robot* 2021;6:eaay2627.
 36. Wehner M, Truby RL, Fitzgerald DJ, *et al.* An integrated design and fabrication strategy for entirely soft, autonomous robots. *Nature* 2016;536:451–455.
 37. Regnault G, Mauger C, Blanc-Benon P, *et al.* Secondary radiation force between two closely spaced acoustic bubbles. *Phys Rev E* 2020;102:31101.
 38. Doinikov AA (eds). Bjerkness forces and translational bubble dynamics. In: *Bubble and Particle Dynamics in Acoustic Fields: Modern Trends and Applications*. Kerala, India: Research Singpost, 2005.
 39. Bertin N, Spelman TA, Combriat T, *et al.* Bubble-based acoustic micropulsors: Active surfaces and mixers. *Lab Chip* 2017;17:1515–1528.
 40. Bertin N, Spelman TA, Stephan O, *et al.* Propulsion of bubble-based acoustic microswimmers. *Phys Rev Appl* 2015;4:1–5.
 41. Ahmed D, Ozcelik A, Bojanala N, *et al.* Rotational manipulation of single cells and organisms using acoustic waves. *Nat Commun* 2016;7:11085.
 42. Ahmed D, Lu M, Nourhani A, *et al.* Selectively manipulable acoustic-powered microswimmers. *Sci Rep* 2015;5:9744.
 43. Qiu T, Adams F, Palagi S, *et al.* Wireless acoustic-surface actuators for miniaturized endoscopes. *ACS Appl Mater Interfaces* 2017;9:42536–42543.
 44. Ren L, Nama N, McNeill JM, *et al.* 3D steerable, acoustically powered microswimmers for single-particle manipulation. *Sci Adv* 2019;5:eaax3084.
 45. Aghakhani A, Yasa O, Wrede P, *et al.* Acoustically powered surface-slipping mobile microrobots. *Proc Natl Acad Sci U S A* 2020;117:3469–3477.
 46. Acevedo R, Restaino MA, Yu D, *et al.* 3D nanoprinted liquid-core-shell microparticles. *J Microelectromechanical Syst* 2020;29:924–929.
 47. Hippler M, Weißenbruch K, Richler K, *et al.* Mechanical stimulation of single cells by reversible host-guest interactions in 3D microscavolds. *Sci Adv* 2020;6:eabc2648.
 48. Doinikov AA, Bouakaz A. Acoustic microstreaming around a gas bubble. *J Acoust Soc Am* 2010;127:703–709.
 49. Dolev A, Kaynak M, Sakar MS. Dynamics of entrapped microbubbles with multiple openings. *Phys Fluids* 2022;34:012012.
 50. Audoly B, Pomeau Y. *Elasticity and Geometry: From Hair Curls to the Non-Linear Response of Shells*. Oxford, UK: Oxford University Press, 2010.
 51. Howell LL, Magleby SP, Olsen BM. *Handbook of Compliant Mechanisms*. West Sussex, UK: John Wiley & Sons, 2013.
 52. Guseinov R, McMahan C, Pérez J, *et al.* Programming temporal morphing of self-actuated shells. *Nat Commun* 2020;11:1–7.
 53. Gelderblom H, Zijlstra AG, van Wijngaarden L, *et al.* Oscillations of a gas pocket on a liquid-covered solid surface. *Phys Fluids* 2012;24:122101.
 54. Bruus H. Acoustofluidics 7: The acoustic radiation force on small particles. *Lab Chip* 2012;12:1014–1021.
 55. Barnkob R, Augustsson P, Laurell T, *et al.* Measuring the local pressure amplitude in microchannel acoustophoresis. *Lab Chip* 2010;10:563–570.
 56. Guizar-Sicairos M, Thurman ST, Fienup JR. Efficient subpixel image registration algorithms. *Opt Lett* 2008;33:156.
 57. Gill PE, Murray W, Wright MH. *Practical optimization*. Philadelphia, USA: Society for Industrial and Applied Mathematics 2019.
 58. Doinikov AA, Zavtrak ST. On the mutual interaction of two gas bubbles in a sound field. *Phys Fluids* 1995;7:1923–1930.
 59. Bruus H. Acoustofluidics 10: Scaling laws in acoustophoresis. *Lab Chip* 2012;12:1578–1586.
 60. Zhang W-M, Yan H, Peng Z-K, *et al.* Electrostatic pull-in instability in MEMS/NEMS: A review. *Sens Actuat A Phys* 2014;214:187–214218.
 61. Novelino LS, Ze Q, Wu S, *et al.* Untethered control of functional origami microrobots with distributed actuation. *Proc Natl Acad Sci U S A* 2020;117:24096–24101.
 62. Chen T, Pauly M, Reis PM. A reprogrammable mechanical metamaterial with stable memory. *Nature* 2021;589:386–390.
 63. Hu X, Yasa IC, Ren Z, *et al.* Magnetic soft micromachines made of linked microactuator networks. *Sci Adv* 2021;7:1–10.
 64. Hippler M, Blasco E, Qu J, *et al.* Controlling the shape of 3D microstructures by temperature and light. *Nat Commun* 2019;10:1–8.
 65. Nishiguchi A, Mourran A, Zhang H, *et al.* In-gel direct laser writing for 3D-designed hydrogel composites that undergo complex self-shaping. *Adv Sci* 2018;5:1700038.
 66. Pancaldi L, Dirix P, Fanelli A, *et al.* Flow driven robotic navigation of microengineered endovascular probes. *Nat Commun* 2020;11:6356.
 67. Zhang Y, Castro DC, Han Y, *et al.* Battery-free, lightweight, injectable microsystem for in vivo wireless pharmacology and optogenetics. *Proc Natl Acad Sci U S A* 2019;116:21427–21437.
 68. Coullais C, Teomy E, de Reus K, *et al.* Combinatorial design of textured mechanical metamaterials. *Nature* 2016;535:529–532.
 69. Overvelde JTB, Weaver JC, Hoberman C, *et al.* Rational design of reconfigurable prismatic architected materials. *Nature* 2017;541:347–352.
 70. Iniguez-Rabago A, Li Y, Overvelde JTB. Exploring multistability in prismatic metamaterials through local actuation. *Nat Commun* 2019;10:5577.

Address correspondence to:

Mahmut Selman Sakar
 Institute of Mechanical Engineering
 Ecole Polytechnique Fédérale de Lausanne
 MED3 2916 Station 9
 CH-1015 Lausanne
 Switzerland

E-mail: selman.sakar@epfl.ch